U(VI) sorption and reduction kinetics on the magnetite (111) surface

David M. Singer[*1,2], *Shawn M. Chatman*[3], *Eugene S. Ilton*[3], *Kevin M. Rosso*[3], *Jillian F. Banfield*[1], *and Glenn A. Waychunas*[2]

1. Department Earth & Planetary Sciences, University of California, Berkeley

2. Earth Sciences Division, Lawrence Berkeley National Laboratory

3. Fundamental and Computational Sciences Directorate, Pacific Northwest National Laboratory

*Corresponding author: dmsinger@lbl.gov

ABSTRACT: Sorption of contaminants onto mineral surfaces is an important process that can restrict their transport in the environment. In the current study, uranium (U) uptake on magnetite (111) was measured as a function of time and solution composition (pH, $[CO_3]_T$, [Ca]) under continuous batch-flow conditions. We observed, in real-time and *in situ*, adsorption and reduction of U(VI) and subsequent growth of UO_2 nanoprecipitates using atomic force microscopy (AFM) and newly developed batch-flow U L_{III}-edge grazing-incidence x-ray absorption spectroscopy near-edge structure (GI-XANES) spectroscopy. U(VI) reduction occurred with and without CO_3 present, and coincided with nucleation and growth of UO_2 particles. When Ca and CO_3 were both present no U(VI) reduction occurred and the U surface loading was lower. *In situ* batch-flow AFM data indicated that UO_2 particles achieved a maximum height of 4-5 nm after about 8 hours of exposure, however, aggregates continued to grow laterally after 8 hours reaching up to about 300 nm in diameter. The combination of techniques indicated that U uptake is divided into three-stages; (1) initial adsorption of U(VI), (2) reduction of U(VI) to UO_2 nanoprecipitates at surface-specific sites after 2-3 hours of exposure, and (3) completion of U(VI) reduction after ~6-8 hours. U(VI) reduction also corresponded to detectable increases in Fe released to solution and surface topography changes. Redox reactions are proposed that explicitly couple the reduction of U(VI) to enhanced release of Fe(II) from magnetite. Although counter intuitive, the proposed reaction stoichiometry was shown to be largely consistent with the experimental results. In addition to providing molecular-scale details about U sorption on magnetite, this work also presents novel advances for collecting surface sensitive molecular-scale information in real-time under batch-flow conditions.

INTRODUCTION

Much research has gone into understanding the (bio)geochemical cycling of uranium (U) in terrestrial environments and processes affecting its migration. Uranium in the environment is usually found in two redox states; U(VI), which is soluble and mobile (as the uranyl moiety UO_2^{2+}) and U(IV), which is relatively insoluble and usually precipitates as uranium dioxide (the mineral uraninite, UO_2). It is generally accepted that processes which result in the transformation of U(VI) to U(IV) effectively sequester uranium in the environment.[1] One important pathway for U(VI) reduction is by Fe(II)-bearing minerals, particularly magnetite[2]. Magnetite is relevant to contaminated and natural environments[3, 4], corrosion of steel, glass, and other waste forms in high-level radioactive waste canisters[5, 6], and groundwater remediation projects[7-9], where it has been shown to have an important role in mediating redox cycling of U and other heavy metals and radionuclides.

Developing accurate predictive models for the fate of U in these environments is predicated in part on understanding the fundamental, molecular-scale controls on U(VI) sorption and reduction kinetics at Fe(II)-bearing surfaces such as magnetite. This is complicated by the fact that multiple U(VI) uptake pathways can be present simultaneously, including: (1) non-reductive U(VI) adsorption; (2) U(VI) adsorption onto or incorporation within a secondary Fe(III)-(oxy)hydroxides[10]; and (3) heterogeneous reduction of U(VI) to U(IV) by structural or adsorbed Fe(II).[11-14] The availability of multiple uptake pathways has so far impeded reliable U(VI) reduction rate prediction in such systems.

Latta et al. (2012) have shown that magnetite stoichiometry, which can be restored by the sorption of aqueous Fe(II), is a critical determinant for the reduction of U(VI) by magnetite.[15] More generally, the availability of Fe(II) at the mineral-water interface, either as the result of adsorption or in surface sites, can impact the extent of U(VI) reduction, ranging from complete to partial reduction.[13, 16-21] Studies to date have provided U(VI) reduction rates for a wide range of solution conditions and mineral characteristics. However, a molecular-scale view of the process is lacking. This knowledge gap may be addressed using single crystal experiments, where the surface structure can be well characterized using, for example, grazing incidence (GI) synchrotron measurements, and the nature of sorption complexes can be determined.[22] Incorporation of fluid flow in such experiments has so far been limited but is nonetheless required to approximate relevant environmental conditions, and recent developments in experimental design have allowed for greater control over flow conditions during surface-sensitive sorption experiments.[23] However, in situ GI observations in real-time from initial exposure of the surface to a reactant through all phases of uptake have not been achieved.

Using a combination of benchtop sorption experiments, atomic force microscopy (AFM), and synchrotron-based grazing-incidence x-ray absorption spectroscopy (GI-XAS), we have measured U(VI) uptake on magnetite (111) as a function of time and solution composition (pH, $[CO_3]$, [Ca]) under continuous batch-flow conditions. To our knowledge the GI-XANES experiments represent the first *in situ*, continuous batch-flow experiments for determining actinide uptake on a mineral surface. This suite of techniques enabled determination of the structure, composition, and morphology of U-bearing surface phases ranging from adsorption complexes to reduced U-bearing precipitates and a detailed analysis of the kinetics of U uptake by multiple uptake pathways.

MATERIALS AND METHODS

Magnetite preparation and characterization Magnetite (111) surface preparation details can be found in Singer et al.[24] In brief, high purity natural Fe_3O_4 single crystals were oriented, cut, and surfaces were prepared by chemical-mechanical polishing (CMP) to a low RMS roughness (≤ 1.5 nm). The prepared crystals were kept under N_2 prior to the batch-flow experiments, and crystals used within two days of CMP showed no evidence of oxidation prior to the batch-flow experiments, as determined by x-ray photoelectron spectroscopy (XPS). The surface area values for the crystals used in the batch-flow experiments are reported in SI Table 1.

Batch-flow sorption experiments Uptake of U(VI) onto the magnetite (111) surface was determined as a function of time and solution composition. Prepared crystals were placed in a 30 mL Nalgene bottle connected to a peristaltic pump by Tygon tubing with 0.2 μm filters connected to the inlet and outlet port of the Nalgene bottle, with the solutions recirculated under batch-flow conditions at a rate of 5 μL/s using 25 mL of solution. Solution conditions were as follows; pH 5 or 10, 0.1 mM U(VI) (introduced as uranyl nitrate), 1 mM $NaNO_3$, $[CO_3]_T$ = 0 or 0.5 mM (introduced as $NaHCO_3$), and [Ca] = 0 or 0.1 mM (introduced as $CaCl_2$). Solubility and aqueous speciation calculations were performed with Visual MINTEQ, version 5.52[25] using a U(VI) thermodynamic database[26], with supplementary thermodynamic data for U(VI)-CO_3 aqueous complexes[27] and U(VI)-CO_3-Ca aqueous complexes.[28] At pH 5 the dominant U(VI) solution species were calculated to be U(VI)-hydrolysis products, dominated by $(UO_2)_3(OH)_5^+$,

independent of the presence of CO_3 and Ca. At pH 10 with no CO_3 and no Ca present, the dominant U(VI) solution species were; $(UO_2)_3(OH)_7^-$ (59.8 %) and $UO_2(OH)_3^-$ (39.4 %); with CO_3 and no Ca present $UO_2(CO_3)_3^{-4}$ (56.4 %), $UO_2(OH)_3^-$ (25.5 %), and $(UO_2)_3(OH)_7^-$ (15.8 %); with CO_3 and Ca present $CaUO_2(CO_3)_3^{-2}$ (56.0 %), $UO_2(CO_3)_3^{-4}$ (18.2 %), and $UO_2(OH)_3^-$ (16.5 %). The saturation index value for all relevant phases (schoepite, rutherfordine, liebigite, and calcite) were all < 0 under all sets of conditions. All solutions were prepared using N_2-purged H_2O (dissolved O_2 < 0.01 ppm), and all batch-flow experiments were setup in a Coy Laboratories, Inc. anoxic chamber (2% H_2/98% N_2, < 0.1 ppm O_2). The solutions were not buffered in order to avoid any interference between an organic buffer and U(VI) adsorption. Over the course of the experiment, the pH increased from 5.00 to 5.10 (± 0.05) and from 10.00 to 10.05 (± 0.05), for all solution compositions. The effluent was sampled in 0.5 mL aliquots which were centrifuged (Eppendorf 5810R) for 10 minutes at 10k rpm and passed through a 20 nm filter and then acidified. Aqueous U and Fe concentrations were determined using a Perkin Elmer SCIEX Elan DRC II Inductively Coupled Plasma Mass Spectrometer (ICP-MS). Background Fe in solution was determined by exposing magnetite (111) crystals to the electrolyte solution in the absence of U(VI) for each solution condition (i.e. pH 5 or 10, with and without CO_3/Ca). Changes in aqueous Fe were measured over the same timeframe as the U(VI) sorption experiments. The ICP-MS detection limits for U and Fe are 0.001 ppb and 0.01 ppb, respectively, and the average uncertainty (two standard deviations) for the current experiments for U and Fe are ± 1 ppm and ± 5 ppm, respectively. The solution conditions (pH, [U], [CO_3], [Ca]) for the sorption experiment were the same used for the batch-flow AFM and GI-XAS experiments; reaction vessel volume, solution volume, and flow rates are stated below for the batch-flow AFM and GI-XAS experiments.

In situ *batch-flow Atomic force microscopy* *In situ* AFM images were obtained at the Environmental Molecular Sciences Laboratory using a Dimension Icon AFM (Veeco Instruments Inc.) in contact mode with contact forces routinely minimized upon engagement before imaging. Magnetite samples were transferred under N_2, and the AFM chamber was continuously purged with N_2 during sample changes and analysis. AFM images were acquired using silicon nitride tips (NP-10 and/or SNL-10; Bruker Corp.) with a spring constant of 0.35 Nm^{-1} and resonance frequency of 65 kHz for both tip types. Image pixel density was 2560 x 2560 lines and scan sizes ranged from 0.1 to 25 μm. Magnetite samples were mounted in a custom flow-cell (5 mL capacity) which was connected with Tygon tubing to a peristaltic pump outside of the AFM chamber (SI Fig. 1) with a total solution volume of 25 mL which filled the total tube length used. AFM images were collected under continuous batch flow conditions (3 μL/s) with no noise apparent in the data due to fluid pumping. Evaporation from the flow-cell within the AFM chamber was minimal and the reservoir volume never decreased by more than 10% over the course of each run and the solutions remained undersaturated. AFM images were collected continuously for 24 hr, and the sample position was periodically adjusted for drift (~ 0.1 - 0.5 μm/hr). Images were processed using the NanoScope v.8 Software (Veeco Instruments Inc.) using a 0^{th} order flattening procedure.

In situ *batch-flow grazing-incidence x-ray absorption spectroscopy* U L_{III}-edge grazing-incidence x-ray absorption near edge structure (GI-XANES) spectra were collected at room temperature at beamline 11-2 at the Stanford Synchrotron Radiation Lightsource (SSRL).[29]

CMP-prepared magnetite (111) samples were run under continuous batch-flow conditions similar to the sorption and AFM experiments, to collect GI-XANES spectra as a function of reaction time, using a sample cell designed for flow reactions using actinide-bearing solutions in an inert atmosphere (SI Fig. 2). Batch-flow samples were mounted on anodized Al sample platforms, with partial o-rings on either side of the crystals to support a 25 μm Kapton film which is held in place by an anodized Al frame. The entire sample cell was placed within a modified AnaeroPack box, with x-ray transparent windows (25 μm Kapton film) cut into the sides. The sample box functioned as both secondary containment for the liquid actinide sample and as an inert, (anoxic and, as needed, low-CO_2) environment for the samples. A peristaltic pump (Welco Co. Ltd., model VPX-1) was mounted on one wall of the sample box, and sealed with rubber o-rings at both the pump head and mounting screw locations. The sample cell, solution reservoir (25 mL total solution volume in a 30 mL Nalgene bottle), and peristaltic pump were connected by Tygon tubing and data was collected under constant flow conditions (5 μL/s). The sample cell and containment box were prepared in the anoxic chamber, and an O_2-scrubbing catalyst (Mitsubishi Gas Chemical Co.) was placed inside the sample box, which remained active during sample transportation and data collection, as evidenced by the fact that the catalysts packs were still warm to the touch after completing data collection for a given sample.

GI-XAS data was collected using a cryogenically cooled Si(220), $\phi = 90^{o}$, double-crystal monochromator. Fluorescence-yield data were collected using a high-throughput 30-element solid-state germanium array detector. The incident beam was defined by 50 μm vertical slits upstream of the sample. A collimating mirror before the monochromator was used for harmonic rejection, with a cutoff of 22 keV. For all grazing-incidence experiments, the angle of the

incident x-rays to the crystal surfaces was set to 0.12°, which is less than the critical angle of the substrate over the energy range examined. X-ray energy was calibrated using yttrium foil; the first inflection point in the Y K-edge was set to 17038 eV. The U L_{III}-edge position was set as the half-height of the normalized adsorption edges. The dominant U oxidation state(s) determination was based on the calibrated edge position with respect to uraninite and uranyl nitrate mechanical mixture standards with an uncertainty of the oxidation state by ± 5 %.[30] Background subtraction, normalization, and data analysis was performed using SixPACK.[31]

RESULTS AND DISCUSSION

Nanoparticulate UO_2 growth and U(VI) reduction rates In a companion paper,[24] nanoparticulate UO_2 was identified on the magnetite (111) surface, using a combination of SEM and GI-XRD, after 12 hours of reaction with aqueous U(VI) in parallel batch experiments. Scanning electron microscopy indicated that the smallest particles were roughly spherical with a 5 nm diameter, occurring in aggregate clusters on the order of 50-100 nm in lateral range. Under batch-flow conditions in the current work, particles were observed by AFM to develop on the magnetite (111) surface within 2 hours, primarily on and adjacent to topographically negative linear surface features, interpreted to be predominantly structural domain boundaries and, to a lesser extent, cracks and scratches (Fig. 1, SI Fig. 3). Evidence for U(VI) reduction over the same time frame was provided by the batch-flow GI-XANES spectra (Fig. 2). In the absence of Ca, the U L_{III}-edge shifted over the course of the flow experiment from U(VI) towards U(IV). The position of the edge between U(VI) and U(IV) at the end of the experiment was shown to be due to the presence of both adsorbed U(VI) and nanoparticulate UO_2, and not the presence of a

mixed-valent phase.[24] When both CO_3 and Ca were present in solution, U(VI)-CO_3-Ca sorption complexes[24] formed and no U(VI) reduction occurred, with a corresponding lack of particle formation observed in the AFM images and no shift in the U L_{III}-edge position in GI-XANES spectra. When reduction did occur, nanoparticulate UO_2 particle size and growth rates were independent of the initial solution composition, i.e., pH and the presence or absence of CO_3 (Fig. 1). Particle height and diameter values in Figure 1 represent mean values from an AFM image for a given time point, and do not differentiate individual particles from particle aggregates. The smallest particles observed in the batch-flow AFM experiments after 2-3 hours of exposure had dimensions of 1-2 nm vertically and 50-100 nm laterally. Given the higher vertical resolution compared to the tip-curvature-limited lateral resolution in the AFM data, and conversely the better lateral versus vertical resolution in the SEM analysis discussed previously, the diameter of the earliest formed particles is therefore most likely on the order of 1 nm, which then coalesce to form larger aggregates. The process of aggregate formation could be the result of: (1) nucleation of new UO_2 particles which aggregate to previously precipitated particles and/or (2) precipitation of new particles on existing UO_2 particles and the continued growth of 'super particle' clusters. In sequences of AFM images, nucleation of individual UO_2 particles was observed, followed by continued growth in the form of aggregates; < 1 nm particles and/or precipitation at new nucleation sites was not observed at later time points following the initial onset of UO_2 precipitation. Particle/aggregate growth therefore proceeds via the formation of 'super particle' clusters from primary particles, and not secondary particle precipitation followed by particle transport-based aggregation. Particle aggregates quickly grew to 100 nm laterally within 8 hours, and then continued growth at a slower rate. Within 24 hours, lateral growth stopped when aggregates reached 200-300 nm. In contrast, vertical growth was limited to 4-5 nm, and ceased

after 8 hours. These results are consistent with the formation of a passivating layer during metal reduction.[32-34]

Nanoparticulate UO_2 growth rates observed by AFM are consistent with U(VI) reduction rates determined by the GI-XANES analysis; the U L_{III}-edge position moves to lower energy values within 2-4 hours after exposure of U(VI) to the magnetite (111) surface (Fig. 2) but reached a plateau around 8 hours, roughly the same time that the AFM data indicated slowing precipitate formation. It is possible that some U(VI) reduction and UO_2 precipitation occurred within the first two hours of exposure. However, early reduction may be undetectable because the concentration of U(IV) was low relative to adsorbed U(VI), making detection of U(IV) difficult via GI-XANES. Furthermore, particles that project less than 1 nm above the average height of the surface would be difficult to image using AFM, given the RMS roughness of the CMP-prepared surface.

The batch-flow sorption trends (Fig. 3) indicate continual U uptake over the first 4 hours, suggesting that there was a possible lag in U(VI) reduction, within the detection limit of GI-XANES as discussed above, compared to adsorption on the magnetite (111) surface (discussed below). Under one set of solution conditions (pH 10, no CO_3 and no Ca), the U L_{III}-edge position appears to have rebounded slightly toward U(VI) after 16 hours of flow-through exposure. Although the edge position after this point is within the error limits of the relatively stable edge position in the 10 hours prior, partial U re-oxidation may have occurred. This was the first batch-flow experiment performed, when the experimental setup was still being optimized, and it is possible that a small amount of O_2 entered the system and resulted in the slight re-oxidation of U toward to end of the experiment. However, there was no corresponding

decrease in particle size observed in the AFM images in this time range, as might be expected from oxidative dissolution of U(IV) from the surface precipitates.

U(VI) adsorption rates and surface Fe release Total U(VI) uptake by the magnetite (111) surface and changes in solution Fe concentration were determined under continuous batch-flow conditions (Fig. 3). When U(VI) reduction occurred at both pH 5 and 10 (i.e., when CO_3 and Ca were both absent), the total U sorption loading was higher than when U(VI) reduction did not occur. The observed total U sorption trends clearly indicate that U(VI) reduction provides a second pathway for increased total U uptake on the magnetite (111) surface in addition to U(VI) adsorption. The onset of U(VI) reduction, observed in the GI-XANES data after 2-4 hours, does not seem to have a significant impact on the rate of U uptake, with no apparent change in slope of the sorption curves over this timeframe. This may be due to the combined effects of slowing U(VI) adsorption as U(VI) reduction begins. However, the overall slope of the uptake curve is steeper when U(VI) adsorption and reduction occurs compared to adsorption only, i.e., in the CO_3-Ca-bearing system. Consequently, the sorption trends for the CO_3-Ca system can be used to roughly approximate the background U(VI) adsorption trends at pH 5 and 10 during reduction. Given this assumption, the ratio of reduced U to adsorbed U is approximately 2:3 after 8 hours of reaction time, which is consistent with the 8 hour U L_{III}-edge position in the GI-XANES data (Fig. 2). Further, the U(VI) reduction rate can be extracted from the total U adsorption loadings by subtracting the sorption trends in the CO_3-Ca-bearing system at a given pH from the sorption trends during U(VI) reduction. Although this approach assumes that the U(VI) adsorption behavior in the absence or presence of CO_3 is the same as the CO_3-Ca-bearing system, it allows

for a reasonable approximation of the adsorption-independent reduction rate. Based on this approach, from the onset of U reduction which was roughly linear through 8 hours of exposure, the first-order rate coefficients, k_{obs} (where $[U] = [U]_0 e^{-kt}$) for U(VI) reduction are 0.1 min^{-1} (pH 5) and 0.06 min^{-1} (pH 10).

The presence or absence of U(VI) reduction during uptake is correlated with the aqueous Fe concentration (Fig. 3). In the absence of U(VI) reduction, Fe released into solution over the background (i.e., same solution composition but with no U(VI) present) was minimal. In contrast, when U(VI) reduction did occur the amount of Fe released was 10x and 5x above the background at pH 5 and pH 10, respectively. The enhanced dissolution of magnetite was also observed during the interaction of U(VI) with nano-magnetite.[35] The amount of Fe lost from the magnetite surface during exposure to U(VI) was independently estimated by quantifying changes in the surface topography based on AFM. Upon exposure of the magnetite crystal to an electrolyte solution prior to U(VI) exposure, a small amount of dissolution released Fe into solution. This Fe background, accounted for in the batch-flow sorption experiments, manifested in the AFM images as deepening of surface features, including domain boundaries, cracks and scratches. The amount of Fe released, and the corresponding roughening of the surface topography typically reached steady-state within 10 minutes, although a small amount of Fe continued to be released during U(VI) adsorption (Fig. 3; CO_3-Ca-bearing systems). In contrast, when U(VI) reduction occurred, the amount of Fe released increased, and coincided with continued surface roughening (Fig. 4). Selected AFM cross-sections documenting these changes are representative for each solution composition, and the respective trends were reproduced in replicate experiments. These trends are consistent with the batch-flow sorption experiments, where additional Fe was released into solution when U(VI) reduction occurred. The amount of

Fe lost from the surface was estimated from the AFM images by coupling the measured change in volume of the magnetite surface features, relative to the flat surrounding surface, with surface feature densities estimated at about 10 – 20 % surface coverage. The analyses at both pH 5 and 10 yield results that are consistent with the ICP data for Fe released from the surface (Fig. 3). Data analysis when no U(VI) reduction occurred was challenging due to the small change in aqueous Fe concentration, and it is not surprising that the AFM-based Fe loss estimate would also be less accurate for these conditions.

The correlation between Fe released and U reduction reinforces the expectation that U(VI) reduction is coupled to Fe(II) oxidation, and is thus limited by the availability of Fe(II) sites at the magnetite surface, including the potential resupply of electron equivalents from the bulk crystal. Based on the dominant aqueous species predicted in solution, the overall reaction at pH 5 is:

$$(UO_2)_3(OH)_5^+ + 9Fe_3O_4 \rightarrow 3UO_2 + 12Fe_2O_3 + 3Fe^{2+} + 5OH^-$$

At pH 10 in the absence of carbonate:

$$(UO_2)_3(OH)_7^- + 9Fe_3O_4 \rightarrow 3UO_2 + 12Fe_2O_3 + 3FeOH^+ + 4OH^-$$

$$UO_2(OH)_3^- + 3Fe_3O_4 \rightarrow UO_2 + 4Fe_2O_3 + FeOH^+ + 2OH^-$$

At pH 10 in the presence of carbonate:

$$UO_2(CO_3)_3^{-4} + 3Fe_3O_4 + 3H_2O \rightarrow UO_2 + 4Fe_2O_3 + FeOH^+ + 3HCO_3^- + 2OH^-$$

$$UO_2(CO_3)_3^{-4} + 3Fe_3O_4 + H_2O \rightarrow UO_2 + 4Fe_2O_3 + FeOH^+ + 3CO_3^{-2} + H^+$$

These reaction stoichiometries, in particular the enhanced release of Fe(II), are consistent with previous work on the reduction of other aqueous metal cations by magnetite.[36] Further, during U(VI) reduction, magnetite transformation to maghemite results in the release of Fe(II) and a net loss of solid volume given the molar volumes of magnetite and maghemite and the stoichiometry of the reaction, which is consistent with the observed deepening of the surface features over the course of the reaction. The above reactions also predict a 1:1 relationship between U(IV) produced and Fe(II) released. The total amount of U(IV) on the surface can be estimated by using the U(IV)/U_T value from the GI-XANES data for a given time point in the kinetic U(VI) sorption curves (Fig. 3). The estimated U(IV) sorption loading and Fe release curves are remarkably close the 1:1 stoichiometry predicted by the proposed reactions. One potential complication to correlating U(IV) produced and Fe released is that some U sorption on the sides of the magnetite (111) crystals, ~ 1 mm thick, could not be avoided. We could not accurately account for the exposed surface area on the sides of the magnetite crystals due to their rough nature, and these surfaces likely add up to an additional ~ 10-20 % reactive surface area, resulting in an overestimation of the total U sorption loadings. In addition, it is unclear if the U(IV)/UT value determined for the analyzed (111) surface is preserved on other exposed surfaces. A second potential complication correlating Fe(II) released to U(VI) reduction is that the possible partial re-sorption of released Fe(II) at locations distal to the "etch pits" could not be quantified in the current study. Ultimately, the correlation between U(IV) produced on the magnetite (111) surface and Fe released provides strong support for the proposed redox reactions.

Sorption model for U(VI) on magnetite (111) The collective results of the batch-flow sorption, AFM, and GI-XAS experiments suggest a three-stage uptake model for U(VI) on the magnetite (111) surface (SI Fig 4). The first stage, lasting approximately three hours, involves adsorption of U(VI) surface complexes at flat surfaces and in at areas of high structural defect density, such as domain boundaries and cracks. However, we cannot rule out the possibility that reduction below our detection limits occurred during this period, and formation of trace U(IV) monomers and/or oligomers is possible. One technique which could have probed this time and low detection limit regime is grazing incidence small angle x-ray scattering (GI-SAXS).[37] Preliminary GI-SAXS experiments proved unsuccessful due to experimental challenges related to the large path lengths through atmosphere in the sample containment box, resulting in scattering images dominated by atmosphere scatter over the signal from the surface. However, future work aims to develop this technique for similar batch-flow experiments with U-bearing solutions in a controlled environment, similar to the sample containment system used in the current work.

Onset of the second stage, which lasts approximately 6-8 hours, is demarcated by continuous U(VI) uptake as well as detectable heterogeneous U(VI) reduction and the formation of nanoparticulate UO_2 at defect sites, such as domain boundaries and cracks, but not on surrounding flat (111) surfaces. Finally, after ~8 hours, the surface is passivated and the reducing potential of the defect-rich regions is used up; aggregation of nanoparticulate UO_2 ceases and approximately one monolayer of adsorbed U(VI) has formed on the basal surfaces.

The mechanism for sustaining U(VI) reduction by Fe(II) supplied from the surface during continuous UO_2 nucleation and growth is a topic of prospective importance to explaining the

sorption kinetics. The observation that reductive sorption occurs preferentially at topographic features such as domain boundaries and is accompanied by feature deepening and increased released Fe suggests the importance of structural defects in this system.[24] These areas have a higher abundance of strained and therefore possibly less thermodynamically stable surface sites relative to the surrounding flat (111) region. For example, boundary walls may provide adsorbed U(VI) greater access to lattice Fe(II) electron equivalents through enhanced Fe(II) solubility in these regions or enhanced access to edge-sharing <110> Fe_{oct} chains facilitating solid-state charge transport to the surface, or both.[38] More generally, the shallow walls of the phase boundaries and cracks expose vicinal surfaces that likely have an intrinsically higher site reactivities and/or Fe(II)/Fe(III) ratio compared to the flat (111) surface. The domain boundaries on the magnetite (111) surface are thought to be the result of closure domains that minimize the free energy between adjacent internal magnetic domains. Closure domains typically transect the <111> axis, and can be observed on surfaces manifesting as regularly repeating linear features.[39, 40] It is possible that Fe(II) and/or electron mobility and resupply to the surface from deeper within the bulk magnetite crystal occurs preferentially along these boundaries, providing unique conditions for more favorable U(VI) reduction.[24]

After nucleation of UO_2 nanoparticles, further reduction and growth to form aggregates could occur through direct electron transfer to adsorbing U(VI) from lattice or solubilized Fe(II) and/or by conduction of electron equivalents through the UO_2 particles. Uraninite is a semiconductor with an electronic band gap of ~ 1.3 eV.[41] Although the semiconductor properties of nanoparticulate UO_2 are not well known, they have been shown to be non-insulating, as observed by a lack of surface charging during XPS analysis.[42] Vertically limited growth of the UO_2 nanoparticles is evidence for either limited conductivity through the growing

UO_2 overlayer or potentially limited availability of soluble Fe(II) at the uppermost growth front. This passivation effect is similar to formation of Cr(III) rinds on magnetite after reduction of aqueous Cr(VI).[43] At some thickness, transport of electrons to the uppermost growth front of the overlayer is no longer sufficiently efficient to sustain vertical growth. It is thus conceivable that the band gap properties of the overlayer partly control how thick that layer can become. For example, $Cr(III)_2O_3$ is an insulator and has been shown to form 1-2 nm rinds on magnetite after reduction of Cr(VI).[43] In contrast, the semiconducting UO_2 nanoparticles observed in the current study are 4-5 nm thick. Although vertical growth of UO_2 could also be controlled by the availability of released Fe(II), the lack of evidence for Fe(III)-(oxy)hydroxide reaction production[24] suggests that this pathway for electron transport is not relevant. More broadly, additional considerations regarding the possible role of aqueous Fe(II) include the expectation that homogeneous reduction of $U(VI)_{aq}$ by $Fe(II)_{aq}$ to $Fe(III)_{aq}$, without the formation of a stable Fe(III)-(oxy)hydroxide is thermodynamically unfeasible over the range of pH of interest in most environmental systems.[44] Recent work has shown that U(VI) reduction by aqueous Fe(II) can occur under a limited set of conditions, specifically at low pH and with high molar ratios of Fe(II) to U(VI)[45]; however, these conditions are not applicable to the current study. Further, if homogeneous reduction was the dominant process, it could be expected that UO_2 nanoparticles would be randomly dispersed across the surface, and not localized only at defect-rich regions. However, released Fe(II) may play a role in restricting heterogeneous reduction of U(VI) spatially at and adjacent to the defect sites. Gorski and Scherer (2009) and Latta et al. (2012) showed that the addition of aqueous Fe(II) to suspensions of oxidized magnetite resulted in reduction of U(VI) to UO_2, consistent with Fe(II) taken up from solution and increasing the magnetite stoichiometry.[15, 46] Thus as U(VI) reduction proceeds and the magnetite surface

becomes oxidized, the released aqueous Fe(II) could locally recharge the oxidized surface creating new nucleation sites for further UO_2 growth. Because it appears probable that in our system Fe(II) is more soluble at the defect sites relative to the flat (111) surface, the release of Fe(II) could recharge oxidized Fe surface sites nearby allowing for additional U(VI) reduction, and restricting U(VI) reduction to the spatial domain around the defect sites.

It is striking that U reduction did not occur on the basal, defect-free regions of the (111) surface. Calculations by Skomurski et al. (2011) did show that U(VI) reduction on a cluster model representation of the (100) magnetite surface is sensitive to the local Fe(II) density.[21] Considering that the (111) surface is relatively Fe(II) poor, but stable, one can speculated that there is a high activation energy to electron transfer from the bulk to Fe(III) surface sites. Cumulatively, such factors might inhibit U(VI) reduction. In contrast, at defect-rich sites, the local Fe(II) density is higher, and the Fe(II) possibly less stable (i.e., a stronger reductant assuming local disequilibrium) compared to the flat (111) surface. This might not only aid initial reduction, but continued conduction of electrons from the bulk to the surface might be more facile than at the ideal (111) surface. Molecular level characterization of U(VI) interaction with different magnetite surfaces, in particular the (100) surface, should help constrain some of these hypotheses.

In situ synchrotron sorption experiments and environmental relevance One of the limitations in bridging the gap between laboratory-based model studies and field-based observations and analyses has been the development of experimental protocols which can more closely parallel naturally occurring conditions. A continual challenge for synchrotron-based

sorption experiments has been the development of procedures and cells that allow greater complexity compared to bulk sorption samples. Recent advances in experimental protocol include in-situ column studies that monitor contaminant speciation and distribution during continuous flow (e.g.[47, 48]). Detailed, molecular scale surface-based analyses have also been greatly improved by the recent development of a sample cell similar to that used in the present study, which have been designed for use as portable sample cell for *in-situ* x-ray scattering experiments of radioactive or atmosphere sensitive samples.[23] In this setup, a remote controlled solution flow system is integrated into the containment system that allows for time-resolved sorption experiments to be performed at the desired moment before and/or during data collection. In the current work, we have introduced the ability to continuously collect GI-XANES spectra under batch-flow conditions. Although the presence of the water overlayer inhibited the ability to collect GI-EXAFS spectra, we were able to successfully monitor changes to the redox state of U at the magnetite (111) surface in real-time throughout these experiments. In parallel to the batch-flow AFM and benchtop sorption experiments, a vastly improved depiction of the dominant U uptake processes occurring at the surface was obtained, from the initial exposure of the surface to U(VI), through adsorption and reduction, and nucleation and particle growth.

ACKNOWLEDGMENTS

We gratefully acknowledge support from the U.S. Department of Energy, Office of Science, Basic Energy Sciences, Contract No. DE-AC02-05CH11231. Portions of this work were carried out at the Stanford Synchrotron Radiation Lightsource (SSRL) and the Environmental Molecular Sciences Laboratory (EMSL). The authors wish to thank John Bargar

and Joe Rogers at SSRL for technical support, Joern Larsen (LBNL) for ICP analyses, and Steve Ferreira (LBNL machinist) for fabrication of the GI-XAS flow-cell parts. SSRL is a Directorate of SLAC National Accelerator Laboratory and an Office of Science User Facility operated for the U.S. Department of Energy Office of Science by Stanford University. The EMSL is national scientific user facility sponsored by the DOE-BER. KMR and SMC gratefully acknowledge support from the DOE-BER through the Science Focus Area program at Pacific Northwest National Laboratory. ESI acknowledges support from the U.S. Department of Energy's Office of Basic Energy Science, Geosciences Program. Comments from three anonymous reviewers improved this manuscript.

Supporting Information Available

Magnetite (111) crystal surface area values, images of the batch-flow GI-XAS sample cell and containment system, batch-flow AFM images, and a schematic of the proposed model for U uptake on magnetite (111) is included in a Supporting Information document. This material is available free of charge via the Internet at http://pubs.acs.org.

FIGURE CAPTIONS

Figure 1. Average particle diameter (A) and height (B) from continuous batch-flow AFM analysis for magnetite (111) exposed to U(VI)-bearing solutions at pH 5 (open symbols) and pH 10 (closed symbols) with no CO_3 and no Ca (circles) and with CO_3 and no Ca (squares). When both CO_3 and Ca were present in solution, no particle formation was observed. Error bars represent two standard deviations for the average particle diameter and height for all particles identified in a given AFM image. The particle height and diameter values represent mean values from an AFM image for a given time point, and do not differentiate individual particles from particle aggregates.

Figure 2. Edge position of the U L_{III}-edge GI-XANES collected under continuous batch-flow conditions at pH 5 (upper panel) and pH 10 (lower panel) for three sets of solution conditions: no CO_3 and no Ca (circles), with CO_3 and no Ca (squares), with CO_3 and with Ca (triangles). The dashed horizontal lines represent the edge position of U(VI) and U(IV) from schoepite and uraninite, respectively. Error bars represent 2 standard deviations for data points collected in triplicate by running quick scans in addition to one longer XANES scans.

Figure 3. Cumulative U(VI) sorption (left vertical axis values) on magnetite (111) as a function of time (solid symbols), Fe released (open symbols) above background (i.e. compared to magnetite in an electrolyte solution), and estimated U(IV) sorption loading (cross-hair symbols) at pH 5 (upper panel) and pH 10 (lower panel) for three sets of solution conditions: no CO_3 and no Ca (circles), with CO_3 and no Ca (squares), with CO_3 and with Ca (triangles). The percent U(VI) removed from solution (right vertical axis values) is based on an initial U(VI) concentration of 0.1 mM . The amount of Fe released is based on changes in surface topography derived from the batch-flow AFM experiments (gray areas) are estimated by assuming that surface feature coverage ranged from 20 % (dashed lines) and 10 % (solid lines). The estimated U(IV) sorption loadings are based on the percent U(IV) from the GI-XANES data at the equivalent time position; data is not shown for the Ca-CO_3-bearing system, as no U reduction occurred. Error bars represent 2 standard deviations for data points collected in triplicate.

Figure 4. Representative cross-sections from AFM images collected under continuous batch-flow conditions during magnetite (111) exposure to U(VI) at pH 5 (upper panel) and pH 10 (lower panel) with solution composition conditions; with no CO_3 and no Ca (left), with CO_3 and no Ca (middle) and with CO_3 and Ca (right). Cross sections were collected at 0 hours, just prior to exposure to U(VI) (gray lines), and after 4 hours (dashed black line) and 8 hours (solid black line) of exposure to U(VI).

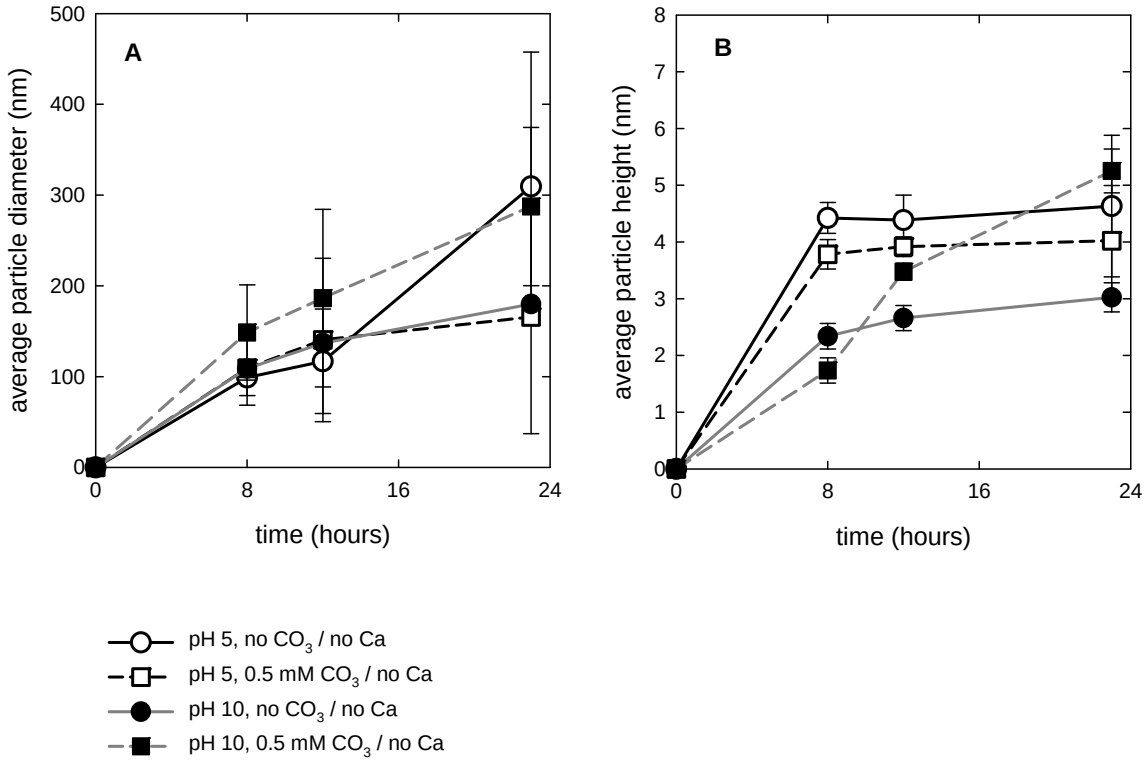

Figure 1. Average particle diameter (A) and height (B) from continuous batch-flow AFM analysis for magnetite (111) exposed to U(VI)-bearing solutions at pH 5 (open symbols) and pH 10 (closed symbols) with no CO_3 and no Ca (circles) and with CO_3 and no Ca (squares). When both CO_3 and Ca were present in solution, no particle formation was observed. Error bars represent two standard deviations for the average particle diameter and height for all particles identified in a given AFM image. The particle height and diameter values represent mean values from an AFM image for a given time point, and do not differentiate individual particles from particle aggregates.

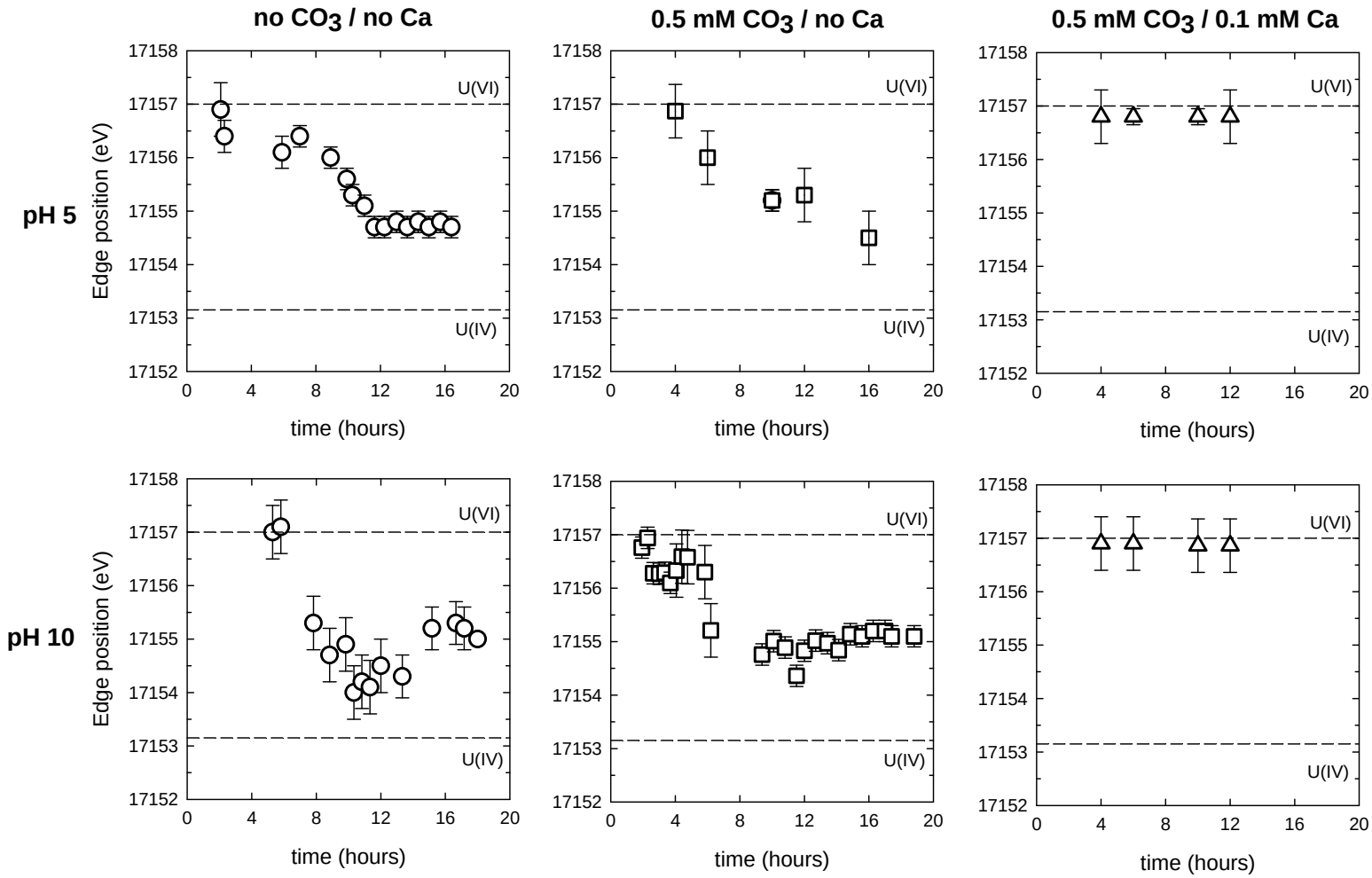

Figure 2. Edge position of the U L_{III}-edge GI-XANES collected under continuous batch-flow conditions at pH 5 (upper panel) and pH 10 (lower panel) for three sets of solution conditions: no CO_3 and no Ca (circles), with CO_3 and no Ca (squares), with CO_3 and with Ca (triangles). The dashed horizontal lines represent the edge position of U(VI) and U(IV) from schoepite and uraninite, respectively. Error bars represent 2 standard deviations for data points collected in triplicate by running quick scans in addition to one longer XANES scans.

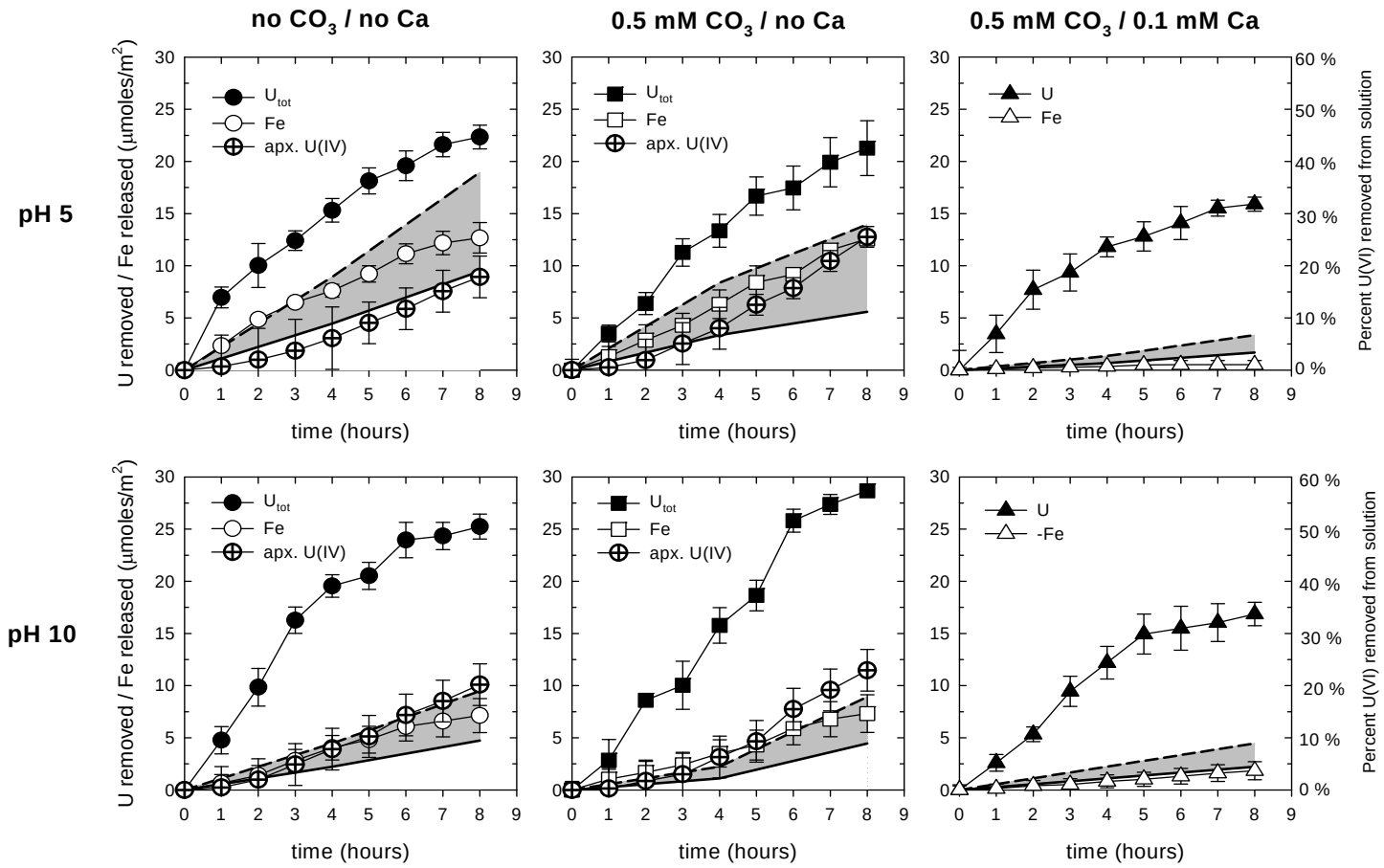

Figure 3. Cumulative U(VI) sorption (left vertical axis values) on magnetite (111) as a function of time (solid symbols), Fe released (open symbols) above background (i.e. compared to magnetite in an electrolyte solution), and estimated U(IV) sorption loading (cross-hair symbols) at pH 5 (upper panel) and pH 10 (lower panel) for three sets of solution conditions: no CO_3 and no Ca (circles), with CO_3 and no Ca (squares), with CO_3 and with Ca (triangles). The percent U(VI) removed from solution (right vertical axis values) is based on an initial U(VI) concentration of 0.1 mM . The amount of Fe released is based on changes in surface topography derived from the batch-flow AFM experiments (gray areas) are estimated by assuming that surface feature coverage ranged from 20 % (dashed lines) and 10 % (solid lines). The estimated U(IV) sorption loadings are based on the percent U(IV) from the GI-XANES data at the equivalent time position; data is not shown for the Ca-CO_3-bearing system, as no U reduction occurred. Error bars represent 2 standard deviations for data points collected in triplicate.

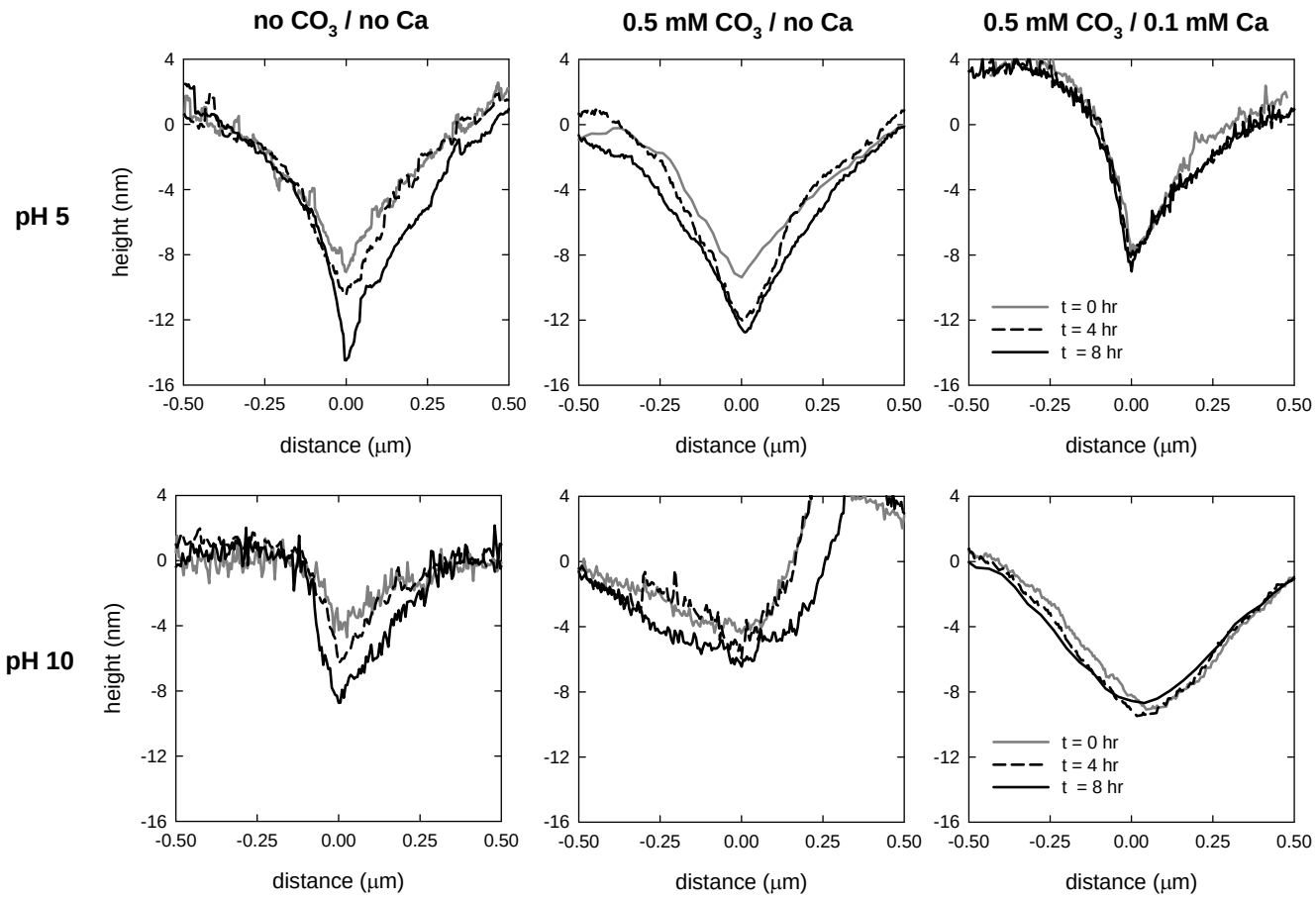

Figure 4. Representative cross-sections from AFM images collected under continuous batch-flow conditions during magnetite (111) exposure to U(VI) at pH 5 (upper panel) and pH 10 (lower panel) with solution composition conditions; with no CO_3 and no Ca (left), with CO_3 and no Ca (middle) and with CO_3 and Ca (right). Cross sections were collected at 0 hours, just prior to exposure to U(VI) (gray lines), and after 4 hours (dashed black line) and 8 hours (solid black line) of exposure to U(VI).

REFERENCES

1. Abdelouas, A.; Lutze, W.; Nuttall, H. E., Uranium contamination in the subsurface; characterization and remediation. *Rev. Mineral. Geochem.* **1999,** *38*, (1), 433-473.
2. Gorski, C. A.; Nurmi, J. T.; Tratnyek, P. G.; Hofstetter, T. B.; Scherer, M. M., Redox behavior of magnetite: Implications for contaminant reduction. *Environ. Sci. Technol.* **2009,** *44*, (1), 55-60.
3. Baik, M. H.; Hyun, S. P.; Cho, W. J.; Hahn, P. S., Contribution of minerals to the sorption of U(VI) on granite. *Radiochim. Acta* **2004,** *92*, 663-669.
4. Singer, D. M.; Zachara, J. M.; Brown Jr, G. E., Uranium speciation as a function of depth in contaminated Hanford sediments - A micro-XRF, micro-XRD, and micro- and bulk-XAFS Study. *Environ. Sci. Technol.* **2009,** *43*, (3), 630-636.
5. Greaves, G. N.; Barrett, N. T.; Antonini, G. M.; Thornley, F. R.; Willis, B. T. M.; Steel, A., Glancing-angle X-ray absorption spectroscopy of corroded borosilicate glass surfaces containing uranium. *JACS* **1989,** *111*, (12), 4313-4324.
6. Duro, L.; El Aamrani, S.; Rovira, M.; de Pablo, J.; Bruno, J., Study of the interaction between U(VI) and the anoxic corrosion products of carbon steel. *Appl. Geochem.* **2008,** *23*, (5), 1094-1100.
7. Abdelouas, A.; Lu, Y. M.; Lutze, W.; Nuttall, H. E., Reduction of U(VI) to U(IV) by indigenous bacteria in contaminated ground water. *J. Contam. Hydrol.* **1998,** *35*, (1-3), 217-233.
8. Wu, W. M.; Carley, J.; Gentry, T.; Ginder-Vogel, M. A.; Fienen, M.; Mehlhorn, T.; Yan, H.; Caroll, S.; Pace, M. N.; Nyman, J.; Luo, J.; Gentile, M. E.; Fields, M. W.; Hickey, R. F.; Gu, B. H.; Watson, D.; Cirpka, O. A.; Zhou, J. Z.; Fendorf, S.; Kitanidis, P. K.; Jardine, P. M.; Criddle, C. S., Pilot-scale in situ bioremedation of uranium in a highly contaminated aquifer. 2. Reduction of U(VI) and geochemical control of U(VI) bioavailability. *Environ. Sci. Technol.* **2006,** *40*, (12), 3986-3995.
9. Yabusaki, S. B.; Fang, Y.; Long, P. E.; Resch, C. T.; Peacock, A. D.; Komlos, J.; Jaffe, P. R.; Morrison, S. J.; Dayvault, R. D.; White, D. C.; Anderson, R. T., Uranium removal from groundwater via in situ biostimulation: Field-scale modeling of transport and biological processes. *J. Contam. Hydrol.* **2007,** *93*, (1-4), 216-235.
10. Duff, M. C.; Coughlin, J. U.; Hunter, D. B., Uranium co-precipitation with iron oxide minerals. *Geochim. Cosmochim. Acta* **2002,** *66*, 3533-3547.
11. Jeon, B.-H.; Dempsey, B. A.; Burgos, W. D.; Barnett, M. O.; Roden, E. E., Chemical reduction of U(VI) by Fe(II) at the solid-water interface using natural and synthetic Fe(III) oxides. *Environ. Sci. Technol.* **2005,** *39*, (15), 5642-5649.
12. Regenspurg, S.; Schild, D.; Schäfer, T.; Huber, F.; Malmström, M. E., Removal of uranium(VI) from the aqueous phase by iron(II) minerals in presence of bicarbonate. *Appl. Geochem.* **2009,** *24*, (9), 1617-1625.
13. Chakraborty, S.; Favre, F.; Banerjee, D.; Scheinost, A. C.; Mullet, M.; Ehrhardt, J.-J.; Brendle, J.; Vidal, L. c.; Charlet, L., U(VI) sorption and reduction by Fe(II) sorbed on montmorillonite. *Environ. Sci. Technol.* **2010,** *44*, (10), 3779-3785.
14. O'Loughlin, E. J.; Kelly, S. D.; Kemner, K. M., XAFS investigation of the interactions of U^{VI} with secondary mineralization products from the bioreduction of Fe^{III} oxides. *Environ. Sci. Technol.* **2010,** *44*, (5), 1656-1661.
15. Latta, D. E.; Gorski, C. A.; Boyanov, M. I.; O'Loughlin, E. J.; Kemner, K. M.; Scherer, M. M., Influence of magnetite stoichiometry on U^{VI} reduction. *Environ. Sci. Technol.* **2012,** *46*, (2), 778-786.
16. Veeramani, H.; Alessi, D. S.; Suvorova, E. I.; Lezama-Pacheco, J. S.; Stubbs, J. E.; Sharp, J. O.; Dippon, U.; Kappler, A.; Bargar, J. R.; Bernier-Latmani, R., Products of abiotic U(VI) reduction by biogenic magnetite and vivianite. *Geochim. Cosmochim. Acta* **2011,** *75*, (9), 2512-2528.
17. Ilton, E. S.; Haiduc, A.; Moses, C. O.; Heald, S. M.; Elbert, D. C.; Veblen, D. R., Heterogeneous reduction of uranyl by micas: Crystal chemical and solution controls. *Geochim. Cosmochim. Acta* **2004,** *68*, (11), 2417-2435.

18. Ilton, E. S.; Haiduc, A.; Cahill, C. L.; Felmy, A. R., Mica surfaces stabilize pentavalent uranium. *Inorg. Chem.* **2005,** *44*, (9), 2986-2988.
19. Ilton, E. S.; Heald, S. M.; Smith, S. C.; Elbert, D.; Liu, C. X., Reduction of uranyl in the interlayer region of low iron micas under anoxic and aerobic conditions. *Environ. Sci. Technol.* **2006,** *40*, (16), 5003-5009.
20. Singer, D. M.; Maher, K.; Brown Jr, G. E., Uranyl-chlorite sorption/desorption: Evaluation of different U(VI) sequestration processes. *Geochim. Cosmochim. Acta* **2009,** *73*, (20), 5989-6007.
21. Skomurski, F. N.; Ilton, E. S.; Engelhard, M. H.; Arey, B. W.; Rosso, K. M., Heterogeneous reduction of U^{6+} by structural Fe^{2+} from theory and experiment. *Geochim. Cosmochim. Acta* **2011,** *75*, 7277-7290.
22. Waychunas, G.; Trainor, T.; Eng, P.; Catalano, J.; Brown Jr, G. E.; Davis, J.; Rogers, J.; Bargar, J., Surface complexation studied via combined grazing-incidence EXAFS and surface diffraction: arsenate on hematite (0001) and (10-12). *Anal. Bioanal. Chem.* **2005,** *383*, (1), 12-27.
23. Schmidt, M.; Eng, P. J.; Stubbs, J. E.; Fenter, P.; Soderholm, L., A new x-ray interface and surface scattering environmental cell design for in situ studies of radioactive and atmosphere-sensitive samples. *Rev. Sci. Instrum.* **2011,** *82*, (7), 075105.
24. Singer, D. M.; Chatman, S. M.; Rosso, K. M.; Ilton, E. S.; Banfield, J. F.; Waychunas, G. A., Identification of simultaneous U(VI) sorption complexes and U(IV) nanoprecipitates on the magnetite (111) surface. *Environ. Sci. Technol.* **2012,** *submitted*.
25. Allison, J. D.; Brown, D. S.; K.J. Novo-Gradac, K. J. *MINTEQA2/PRODEFA2, A geochemical assessment model for environmental systems: Version 3.0 user's manual: EPA/600/3-91/021*; United States Environmental Protection Agency, Office of Research and Development, Washington, D.C.: Washington, D.C., 1991; p 106.
26. Grenthe, I.; Wanner, H.; Forest, I.; OECD Nuclear Energy Agency., *Chemical thermodynamics of uranium*. Elsevier: Amsterdam; New York; New York, N.Y., U.S.A., 1992.
27. Guillaumont, R.; Fanghänel, T.; Fuger, J.; Grenthe, I.; Neck, V.; Palmer, D. A.; Rand, M. H., *Update on the Chemical Thermodynamics of Uranium, Neptunium, Plutonium, Americium and Technetium*. Elsevier: Amsterdam, 2003; Vol. 5.
28. Dong, W.; Brooks, S. C., Determination of the formation constants of ternary complexes of uranyl and carbonate with alkaline earth metals (Mg^{2+}, Ca^{2+}, Sr^{2+}, and Ba^{2+}) using anion exchange method. *Environ. Sci. Technol.* **2006,** *40*, (15), 4689-4695.
29. Bargar, J. R.; Brown Jr., G. E.; Evans, I.; Rabedeau, T.; Rowen, M.; Rogers, J. In *A new hard X-Ray XAFS spectroscopy facility for environmental samples, including actinides, at the Stanford Synchrotron Radiation Laboratory*, Proceedings of the Euroconference and NEA Workshop on Speciation, Techniques, and Facilities for Radioactive Materials at Synchrotron Light Sources, Grenoble, France, Sept. 10-12, 2000, Nuclear Energy Agency/Organization for Economic Cooperation and Development, Paris, 2002; AEN/NEA: Paris, 2002; pp 169-176.
30. Singer, D. M.; Farges, F.; Brown Jr, G. E., Biogenic nanoparticulate UO_2: Synthesis, characterization, and factors affecting surface reactivity. *Geochim. Cosmochim. Acta* **2009,** *73*, (12), 3593-3611.
31. Webb, S., SixPACK: a graphical user interface for XAS analysis using IFEFFIT. *Phys. Scr.* **2004,** *T115*, 1011-1014.
32. Doyle, C. S.; Kendelewicz, T.; Brown Jr, G. E., Inhibition of the reduction of Cr(VI) at the magnetite-water interface by calcium carbonate coatings. *Appl. Surf. Sci.* **2004,** *230*, (1-4), 260-271.
33. Jung, Y.; Choi, J.; Lee, W., Spectroscopic investigation of magnetite surface for the reduction of hexavalent chromium. *Chemosphere* **2007,** *68*, (10), 1968-1975.
34. He, Y. T.; Traina, S. J., Cr(VI) reduction and immobilization by magnetite under alkaline pH conditions: The role of passivation. *Environ. Sci. Technol.* **2005,** *39*, (12), 4499-4504.
35. Ilton, E. S.; Boily, J.-F.; Buck, E. C.; Skomurski, F. N.; Rosso, K. M.; Cahill, C. L.; Bargar, J. R.; Felmy, A. R., Influence of dynamical conditions on the reduction of U^{VI} at the magnetite-solution interface. *Environ. Sci. Technol.* **2010,** *44*, (1), 170-176.

36. White, A. F.; Peterson, M. L., Reduction of aqueous transition metal species on the surfaces of Fe(II) -containing oxides. *Geochim. Cosmochim. Acta* **1996,** *60*, (20), 3799-3814.
37. Jun, Y.-S.; Lee, B.; Waychunas, G. A., In Situ observations of nanoparticle early development kinetics at mineral-water interfaces. *Environ. Sci. Technol.* **2010,** *44*, (21), 8182-8189.
38. Skomurski, F. N.; Kerisit, S.; Rosso, K. M., Structure, charge distribution, and electron hopping dynamics in magnetite (Fe_3O_4) (1 0 0) surfaces from first principles. *Geochim. Cosmochim. Acta* **2010,** *74*, (15), 4234-4248.
39. Özdemir, Ö.; Xu, S.; Dunlop, D. J., Closure domains in magnetite. *J. Geophys. Res.* **1995,** *100*, (B2), 2193-2209.
40. Özdemir, Ö.; Dunlop, D. J., Magnetic domain structures on a natural single crystal of magnetite. *Geophys. Res. Lett.* **1993,** *20*, (17), 1835-1838.
41. Meek, T.; Hu, M.; Haire, M. J., Semiconductive properties of uranium oxides. In *Waste Management 2001 Symposium*, U.S. Department of Energy: Tucson, AZ, 2001.
42. Singer, D. M.; Farges, F.; Brown Jr., G. E., Biogenic UO_2 - characterization and surface reactivity. *Phys. Scr.* **2007,** *882*, (1), 277-279.
43. Peterson, M. L.; White, A. F.; Brown, G. E.; Parks, G. A., Surface passivation of magnetite by reaction with aqueous Cr(VI):□ XAFS and TEM results. *Environ. Sci. Technol.* **1997,** *31*, (5), 1573-1576.
44. Felmy, A. R.; Ilton, E. S.; Rosso, K. M.; Zachara, J. M., Interfacial reactivity of radionuclides: emerging paradigms from molecular-level observations. *Mineral. Mag.* **2011,** *75*, (4), 2379-2391.
45. Du, X.; Boonchayaanant, B.; Wu, W.-M.; Fendorf, S.; Bargar, J.; Criddle, C. S., Reduction of uranium(VI) by soluble iron(II) conforms with thermodynamic predictions. *Environ. Sci. Technol.* **2011,** *45*, (11), 4718-4725.
46. Gorski, C. A.; Scherer, M. M., Influence of magnetite stoichiometry on Fe(II) uptake and nitrobenzene reduction. *Environ. Sci. Technol.* **2009,** *43*, (10), 3675-3680.
47. Komlos, J.; Mishra, B.; Lanzirotti, A.; Myneni, S. C. B.; Jaffe, P. R., Real-time speciation of uranium during active bioremediation and U(IV) reoxidation. *J. Environ. Eng.* **2008,** *134*, (2), 78-86.
48. Tokunaga, T. K.; Wan, J.; Pena, J.; Brodie, E.; Firestone, M. K.; Hazen, T. C.; Sutton, S. R.; Lanzirotti, A.; Newvile, M., Uranium reduction in sediments under diffusion-limited transport of organic carbon. *Environ. Sci. Technol.* **2005,** *39*, (18), 7077-7083.